

Turbulent Torques on Protoplanets in a Dead Zone

Jeffrey S. Oishi^{1,2}, Mordecai-Mark Mac Low², Kristen Menou³

ABSTRACT

Migration of protoplanets in their gaseous host disks may be largely responsible for the observed orbital distribution of extrasolar planets. Recent simulations have shown that the magnetorotational turbulence thought to drive accretion in protoplanetary disks can affect migration by turning it into an orbital random walk. However, these simulations neglected the disk's ionization structure. Low ionization fraction near the midplane of the disk can decouple the magnetic field from the gas, forming a dead zone with reduced or no turbulence. Here, to understand the effect of dead zones on protoplanetary migration, we perform numerical simulations of a small region of a stratified disk with magnetorotational turbulence confined to thin active layers above and below the midplane. Turbulence in the active layers exerts decreased, but still measurable, gravitational torques on a protoplanet located at the disk midplane. We find a decrease of two orders of magnitude in the diffusion coefficient for dead zones with dead-to-active surface density ratios approaching realistic values in protoplanetary disks. This torque arises primarily from density fluctuations within a distance of one scale height of the protoplanet. Turbulent torques have correlation times of only ~ 0.3 orbital periods and apparently time-stationary distributions. These properties are encouraging signs that stochastic methods can be used to determine the orbital evolution of populations of protoplanets under turbulent migration. Our results indicate that dead zones may be dynamically distinct regions for protoplanetary migration.

Subject headings: accretion — MHD — planetary systems: formation — planetary systems: protoplanetary disks — turbulence

¹Department of Astronomy, University of Virginia, P.O. Box 3818, Charlottesville, VA 22903; Email: joishi@amnh.org

²Department of Astrophysics, American Museum of Natural History, Central Park West at 81st St, New York, NY 10024-5192; Email: mordecai@amnh.org

³Department of Astronomy, Columbia University, 550 West 120th St, New York, NY 10027; Email: kristen@astro.columbia.edu

1. Introduction

Detections of extrasolar planets now number in the hundreds (Butler et al. 2006). Their orbital parameters reveal a number of multi-planet systems in mean motion resonances (Lee & Peale 2002; Ji et al. 2003; Lee et al. 2006) and many Jupiter and Neptune-mass objects with major axes under an astronomical unit (Gould et al. 2006). These observations can be explained by orbital migration arising from disk-planet interaction (Lin & Papaloizou 1979; Goldreich & Tremaine 1980).

Protoplanetary migration driven by gravitational interaction with a disk can occur in at least three ways. Type I migration occurs when protoplanets with masses $\lesssim 10 - 30M_{\oplus}$ raise density waves in the disk, which in turn exert torque on the protoplanet (Goldreich & Tremaine 1980). This migration is usually inward due to the radial gradients in pressure, temperature, and sound speed from the global structure of typical disks (Ward 1986). Type II migration is an essentially non-linear process that occurs when a massive planet opens a gap in the surrounding accretion disk (Ward 1997). The planet then couples to the viscous evolution of the disk, migrating inward on the local disk accretion timescale. Type III migration occurs when material in the coorbital region of a roughly Saturnian mass object begins to exert strong corotation torque that scales with the migration rate, leading to runaway (Masset & Papaloizou 2003, though the existence of runaway is questioned by D’Angelo et al. (2005) on resolution grounds). We will here be solely concerned with Type I migration.

For an $\sim 1M_{\oplus}$ object at 5 AU, the time scale for Type I migration is $\tau_{mig} \sim 8 \times 10^5$ yr (e.g., Tanaka, Takeuchi, & Ward 2002), while protoplanetary disks have lifetimes constrained to be less than $t_{disk} \sim 10^7$ yr (e.g., Jayawardhana et al. 2006). This poses a significant challenge to the core-accretion scenario for gas giant planets (Pollack et al. 1996), in which rocky cores take $\sim 10^7$ yr to grow to $\sim 10 - 30M_{\oplus}$ before rapidly accreting a gaseous envelope. Rice & Armitage (2003) note that if a core migrates stochastically, the timescale for core accretion drops by an order of magnitude from this estimate. More recent studies (Hubickyj, Bodenheimer, & Lissaur 2005) show a core-accretion timescale of $1 - 5 \times 10^6$ yr for Jupiter, still considerably longer than the migration timescale.

Essential to this discussion of protoplanetary migration is the disk itself. Disks around young stars are known to be accreting (Hartmann et al. 1998). Angular momentum must be transported outward to allow accretion. The strength of the transport mechanism can be most simply parameterized by the dimensionless viscosity $\alpha = \nu_t / (c_s H)$ (Shakura & Sunyaev 1973). Models incorporating a viscosity characterized by α are known as α -disks. Numerical simulations of disk-planet interaction confirm the basic analytic predictions of the timescales for Type I migration in purely smooth, featureless, laminar disk models in-

cluding α -disks and the minimum mass solar nebula (Miyoshi et al. 1999; Masset 2002; D’Angelo, Kley, & Henning 2003).

However, protoplanetary accretion disks are far from featureless, laminar disks. Recently, two separate approaches to more complex modeling of planet-disk interaction have been identified and pursued. First, more sophisticated one-dimensional α -disk models with radial opacity jumps (Menou & Goodman 2004) and departures from isothermality (Jang-Condell & Sasselov 2005) show that Type I migration rates can be significantly altered by regions of long migration time that function as traps. Additionally, Paardekooper & Mellema (2006) have performed three-dimensional radiation hydrodynamics simulations of Type I migration and found that Type I migration can be halted and even reversed if the disk cannot radiate efficiently in the corotation region of the planet’s orbit. Second, angular momentum transport most likely is actually driven by some form of turbulence, likely the saturated state of the magnetorotational instability (MRI) (see Balbus & Hawley 1998, for a review). Understanding the effects of turbulence on migration requires explicit, three-dimensional, magnetohydrodynamic (MHD) simulations. In a series of recent papers, Nelson, Papaloizou, and collaborators have performed such simulations including the effects of a protoplanet embedded within the turbulent flow (Papaloizou & Nelson 2003; Nelson & Papaloizou 2003; Papaloizou, Nelson, & Snellgrove 2004; Nelson & Papaloizou 2004; Nelson 2005, see also Laughlin, Steinacker, & Adams 2004). These models revealed that for an object with mass $\lesssim 30M_{\oplus}$, torque fluctuations from turbulent density perturbations cause the protoplanet to follow a random walk, possibly significantly lengthening its lifetime.

Johnson, Goodman, & Menou (2006, hereafter JGM06) have argued, using semi-analytic models, that these fluctuations will *decrease* the lifetimes of most planets, but allow a small number of them to scatter to large radii and thus survive. Their approach is based on a Fokker-Planck formalism that treats Type I migration as advection and the orbital motions induced by stochastic torques from turbulence as an independent diffusion process. Such a model depends on details of the turbulence that can only be provided by numerical simulation.

Because protoplanetary disks are cold and dense at their midplanes, the ionization fraction is a strong function of height. The MRI is stabilized by Ohmic diffusion for magnetic Reynolds numbers $Re_M \lesssim 10^4$ for zero-net flux poloidal fields, though the actual value depends strongly on the geometry of the field (Fleming, Stone, & Hawley 2000) and possibly the presence of artificial resistivity (Brandenburg et al. 2004). Therefore, the MRI can not operate at all heights at radii where planet formation likely occurs (Gammie 1996). Modeling of the ionization structure of the disk leads to a three layer description (Gammie 1996; Sano et al. 2000; Fromang et al. 2002; Semenov et al. 2004; Ilgner & Nelson 2006) with MRI

turbulence occurring in active zones above and below a dead zone at the midplane.

Our purpose in this paper is twofold. First, we wish to understand the effect of a dead zone on the migration of a low-mass protoplanet at the midplane. Second, we wish to further quantify the torques on a protoplanet caused by MRI turbulence, with and without dead zones, in order to verify the assumptions of and provide better parameters for the Fokker-Planck model of JGM06.

§ 2 describes our models, § 3 gives a brief overview of the turbulence and dead zones in the plasma, § 4 provides analysis of the torques on protoplanets in real and Fourier space, § 5 discusses the applicability of our results to real disks and statistical treatments of ensembles of migrating protoplanets, and § 6 presents our conclusions.

2. Models

Torques produced by turbulent density perturbations compete with Type I migration in the turbulent migration scenario proposed by Nelson (2005). In order to focus on the characteristics of the turbulence, we exclude active Type I migration in our models by considering a zero-mass test particle fixed at the center of the box. A test particle does not raise density waves in the disk, allowing us to isolate the torques on the planet from disk turbulence. We work in a local frame, allowing for maximum resolution of the disk near the planet—where, as we will show, most of the turbulent torque originates. Our test particle approach has the additional advantage of allowing us to study turbulent migration in the local frame without worrying about spurious density wakes from the (shearing) periodic boundary conditions we employ (eg, Papaloizou et al. 2004; Nelson & Papaloizou 2004). However, in doing so, we implicitly assume that Type I and turbulent torques are separable and additive. It is not clear that this assumption is valid, as Nelson (2005) found that explicit Type I migration in turbulent models differed from the linear combination of stochastic migration on massless protoplanets and a Type I migration rate from laminar disk calculations, suggesting that Type I migration is itself modified by MRI turbulence.

2.1. Numerical Method

We use the Pencil Code¹, a spatially sixth-order and temporally third-order finite difference MHD code (Brandenburg & Dobler 2002) designed to study weakly supersonic turbu-

¹available at <http://www.nordita.dk/software/pencil-code/>

lent flows. The Pencil Code solves the MHD equations in non-conservative form, monitoring conservation as a check on the quality of the solutions.

We work in the shearing box approximation (e.g., Goldreich & Lynden-Bell 1965; Hawley, Gammie, & 1995), in which one considers a small Cartesian box around a fiducial point in the disk at radius R , and expands the gravitational potential from the central protostar to leading order in H/r . The coordinate frame is oriented such that x is the local radial direction, y points in the azimuthal direction, and z is mutually orthogonal. We solve for the departures \mathbf{u} from the mean Keplerian shear flow, $u_y^{(0)} = -3/2\Omega x$. The shearing box MHD equations are thus

$$\partial_t \rho + u_y^{(0)} \partial_y \rho + \nabla \cdot (\rho \mathbf{u}) = f_\rho \quad (1)$$

$$\partial_t \mathbf{u} + \mathbf{u} \cdot \nabla \mathbf{u} + u_y^{(0)} \partial_y \mathbf{u} = -\frac{\nabla P}{\rho} - \nabla \Phi + \frac{\mathbf{J} \times \mathbf{B}}{\rho} + \mathbf{f}_u + 2\Omega u_y \hat{\mathbf{x}} - \frac{\Omega u_x}{2} \hat{\mathbf{y}} - \Omega^2 z \hat{\mathbf{z}} + \zeta (\nabla \nabla \cdot \mathbf{u}) \quad (2)$$

$$\partial_t \mathbf{A} + u_y^{(0)} \partial_y \mathbf{A} = \frac{3\Omega A_y}{2} \hat{\mathbf{x}} + \mathbf{u} \times \mathbf{B} + \eta(z) \mu_0 \mathbf{J} + \mathbf{f}_A \quad (3)$$

where Ω is the rotation rate of the box, f_ρ , \mathbf{f}_u , \mathbf{f}_A are stabilizing hyperdiffusivities (see below), \mathbf{A} is the magnetic vector potential, $\mathbf{J} = \nabla \times \mathbf{B} / \mu_0$ is the current density, $\eta(z)$ is a height-dependent resistivity, and the other symbols have their standard meaning. The extra term $u_y^{(0)} \partial_y$ in all dynamical equations is a result of subtracting the Keplerian shear from the velocity, as is the $(3/2)\Omega A_y$ term in equation (3). Finally, we close the set with an isothermal equation of state,

$$P = c_s^2 \rho, \quad (4)$$

where c_s is the isothermal sound speed.

Because the Pencil Code uses spatially centered finite differences, there is no formal diffusion in the algorithm, so explicit diffusion operators must be included in all dynamical equations in order to ensure numerical stability. In this work, we use sixth order hyperdiffusion for continuity, momentum, and induction, in addition to physical Laplacian (i.e., second order) diffusion. Sixth order hyperdiffusion has the form $\nu_6 \nabla^6 \mathbf{u}$ and damps signals only near the Nyquist wavenumber at the smallest scales of the box, allowing larger modes to remain largely unaffected. Our formulation conserves mass and momentum by construction. For details, we refer the reader to Johansen & Klahr (2005). We capture shocks using a von Neumann artificial viscosity implemented as a bulk diffusion with variable coefficient $\zeta = c \langle \max[(-\nabla \cdot \mathbf{u})_+] \rangle$ (where the max is taken over 3 zones) on the continuity and momentum equations (Haugen, Brandenburg, & Mee 2004).

For our dead zone runs, we have modified the Pencil Code to include a height-dependent resistivity with the profile given by Fleming & Stone (2003):

$$\eta(z) = \eta_0 \exp\left(-\frac{z^2}{2}\right) \exp\left(\frac{\Sigma_0}{\Sigma_{CR}} \frac{1}{2\sqrt{\pi}} \int_z^\infty e^{-z'^2} dz'\right), \quad (5)$$

where $\Sigma_{CR} \simeq 100 \text{ g cm}^{-2}$ is the stopping depth of cosmic rays and Σ_0 is the surface density of the disk. We adopt a value for $\Sigma_0/\Sigma_{CR} = 30$, consistent with FS03 and roughly twice the minimum mass solar nebula value at 1 AU. Note that FS03 incorrectly identify η_0 as the midplane resistivity, rather than $\eta_{\text{mid}} = \eta_0 \exp(\Sigma_0/4\Sigma_{CR})$, though this error does not carry through their calculations of the magnetic Reynolds number (J. Stone 2006, private communication).

2.2. Initial and Boundary Conditions

We initialize the disk in hydrostatic equilibrium in the vertical direction, leading to a density profile $\rho(z) = \rho_0 \exp(-z^2/H^2)$, where $H = \sqrt{2c_s^2/\Omega^2}$ is the scale height of the disk. The initial magnetic field strength is parameterized by the maximum plasma $\beta = 2\mu_0 P_g/B_0^2 = 400$. The field geometry is a zero-net flux vertical field $B_z(x) = B_0 \sin(2\pi x/L_x)$. We measure length in units of the disk scale height, H , time in units of Ω^{-1} (although we plot quantities in terms of the orbital period $t_{\text{orb}} = 2\pi/\Omega$), and set the vacuum permeability $\mu_0 = 1$. Our computational domain has size $(x \times y \times z) = 1 \times 4 \times 4$, with resolutions for the models given in Table 1.

In these units, all simulations have a sound speed $c_s = 7.071 \times 10^{-4}$, rotation rate $\Omega = 10^{-3}$, midplane density $\rho_0 = 1$, and random perturbations in \mathbf{u} with amplitude 1×10^{-6} to seed the MRI. In order to vary the size of the dead zone, we vary η_0 in equation 5, which in turn varies the midplane resistivity. We parameterize the size of the dead zone with the magnetic Reynolds number at the midplane $Re_M = c_s^2/(\eta_{\text{mid}}\Omega)$.

Our boundary conditions are periodic in y , shear periodic in x (Hawley et al. 1995), and periodic in z . While the last is not rigorously accurate for a stratified disk such as ours, previous work (Stone et al. 1996) as well as our own direct comparison to vertical field boundary conditions (Brandenburg et al. 1995) suggest that it does not make a significant difference for the density perturbations driven by the MRI.

2.3. Validity of Zero-mass test particles

We monitor the gravitational force on a zero-mass test particle fixed at the center of the grid. This can be directly translated into a torque for a particle that does not move significantly in radius over the course of the simulation. While fixing the position of the planet over the $\sim 100t_{\text{orb}}$ duration of the simulation is an approximation, Figure 6 of Nelson (2005) shows that zero-mass objects vary their semi-major axes by no more than about 10%

over a similar time span.

If we make the assumption that Type I and turbulent migration are separable, then our analysis will apply more generally to objects of finite mass. However, even if these effects do couple, there exist a class of objects for which our results are valid. Here, we derive a range of masses for objects large enough to neglect gas drag and still small enough to cause negligible density waves.

Stokes’ drag law states that the stopping time of an object larger than the mean free path of the gas it is moving through is

$$\tau_f = \frac{2\rho_s a_s^2}{9\mu}, \quad (6)$$

where ρ_s and a_s are the density and radius of the solid object and μ is the dynamic viscosity of the gas (e.g. Weidenschilling 1977).

In order to determine the mass range in which an object can have both drag force and gravitational back reaction on the disk neglected (ie, a massless particle on a fixed Keplerian orbit), we consider the range of sizes a body with solid density roughly that of Earth, $\rho_s \simeq 3 \text{ g cm}^{-3}$, will have both drag times and Type I migration times on the order of the lifetime of a protoplanetary disk, taken here to be 10^7 yr . The dynamic viscosity of a pure hydrogen gas is $\mu = 5.7 \times 10^{-5} T^{-1/2} \text{ g cm}^{-1} \text{ s}^{-1}$ (Lang 1980). Using an α -disk with $\alpha = 10^{-2}$ and $\dot{M} = 10^{-7} M_\odot \text{ yr}^{-1}$, Ilgner & Nelson (2006) give a midplane value of $T \simeq 100 \text{ K}$. The lower limit, $\tau_f > 10^7 \text{ yr}$ gives a radius $a_s \sim 5.1 \times 10^4 \text{ cm}$ which for a spherical object of the above density yields $m \gtrsim 4 \times 10^{14} \text{ g}$. Type I migration times scale inversely with mass, $\tau_{\text{I}} \sim 8 \times 10^5 (m/M_\oplus)^{-1} \text{ yr}$ (Tanaka et al. 2002), and so the upper mass limit is $m_{\text{max}} \lesssim 10^{26} \text{ g}$. This is a broad range of protoplanet masses, $10^{14} \text{ g} \lesssim m \lesssim 10^{26} \text{ g}$, and suggests our results are relevant even if Type I and turbulent migration are coupled for more massive objects.

3. Plasma Dynamics and Dead Zone Parameters

In our models with finite Re_M , magnetic energy rapidly grows near the midplane after a few orbits, due to the cooperation of magnetic reconnection and shear, in agreement with the results of Fleming & Stone (2003). By 10 orbits, MRI turbulence sets in above and below the midplane, forming active layers surrounding a quiescent (but not motionless) dead zone that persists to the end of the simulation (Figure 1). We define the dead zone to be the region where the horizontally averaged Maxwell stress $-\langle B_x B_y \rangle_{xy}$, has fallen by an order of magnitude from its average value at $\pm 1.5H$. (We use unadorned angle brackets to denote

volume averages, while spatial averages over lower dimension and temporal averages have identifying subscripts.) Using $1.5H$ as our baseline, rather than the grid boundary at $2H$, avoids contamination by the slightly elevated value of the Maxwell stress that we see at the boundary. We have confirmed this effect is a result of the periodic boundary conditions adopted with simulations using other boundary conditions. We calculate the total surface density in the active zones Σ_A and compare that with the surface density of the dead zone Σ_D in Table 1.

In a shearing box, symmetry restricts the net transfer of angular momentum, and thus the accretion rate, to zero. In order to measure the ability of the turbulence to drive accretion, we measure the Maxwell stress, as well as the Reynolds stress $\langle \rho u_x u_y \rangle$. These quantities measure the radial transport of angular momentum by the turbulence (e.g. Brandenburg 1998). Figure 2 shows the turbulent stresses normalized by the initial midplane pressure for each of the medium resolution runs. We see Reynolds stresses significantly exceeding Maxwell stresses in the midplane for all of our dead zone models. FS03 demonstrated that these correlated motions are caused by momentum flux from turbulent overshoot at the boundary layer between dead and active regions.

Our models confirm the finding of FS03 that a significant Reynolds stress remains within the dead zone, even as the size and depth of the dead zone, as defined by the dropping Maxwell stress, increase. Because the criteria used by FS03 to define the dead zone width are not entirely clear, it is difficult to make detailed comparisons between our results and theirs. However, applying our definition of a dead zone to Figure 3 in FS03, which shows Maxwell and Reynolds stresses for a model with $Re_M = 100$, the dead zone extends from $|z| < 0.5$. In our comparable model, the dead zone is located between $-0.35 < z < 0.38$. Given that FS03 report that their $Re_M = 10$ model was unable to sustain MRI turbulence while we were able to run a self-sustaining $Re_M = 3$ model, it is possible that the difference in dead zone widths is a result of the different dissipative properties of our respective codes.

The $Re_M = 3$ case demands special attention. Its vertical distribution of stresses is notably different than those of the other non-ideal runs. First, the Reynolds stress at the midplane is substantially less than in the $Re_M = 30$ and 100 cases, which differ by a factor of a few. Second, the Maxwell stress appears to reach a minimum below 10^{-7} and remain constant over $|z| \lesssim 0.5$, though it occasionally becomes slightly negative and is excluded on the log plot. This behavior occurs in both 32R3 and 64R3 models, as well as for a run in double precision. We note that Figure 5 of Turner et al. (2006) shows similar behavior (though not the negative $-B_x B_y$) in dead zone models computed with the Zeus code.

3.1. Resolution Study

In order to study the effects of numerical resolution on our results, we ran our $Re_M = 30$ model at three resolutions, and all others at two. An overall picture of the MRI is given by its saturation energy or average viscous α value, both of which are shown in Figure 3. A more relevant quantity for our purposes is the temporal root-mean-square (RMS) azimuthal gravitational force ($\langle F_y^2 \rangle_t$)^{0.5} (i.e., torque; see § 4). This quantity is directly responsible for orbital migration and is given in Table 1. Figure 3a shows the RMS torque and dead zone column density ratio Σ_a/Σ_d as a function of resolution. While both are resolution dependent, it appears that their values are converging between the highest two resolution runs. The dimensionless effective viscosity $\alpha = (\langle \rho u_x u_y \rangle - \langle B_x B_y \rangle)/P_0$ and maximum Mach number are given in the upper two panels of Figure 3b. Both quantities reflect the well-known result that higher resolution MRI runs lead to lower turbulent stresses (Fromang & Papaloizou 2007).

The magnetic energy for the high resolution run drops by nearly a factor of 7 between orbits 30 and 50, similar to the simulations of Stone et al. (1996). Decreases in magnetic energy at similar times and on similar timescales occur at all resolutions, although not with such large magnitudes. In the lower resolution models run to longer times, these drops eventually stop occurring, typically by orbit 100 and the model maintains a relatively constant magnetic energy level. The timescale for such an adjustment is curiously long; we hope to examine it more closely in future work. For our purposes here, it is sufficient to note that while resolution effects are present, the *duration* of the simulation may be a greater factor in obtaining robust statistical results (see Winters, Balbus, & Hawley 2003, for a discussion).

4. Migration Torques

Turbulent overdensities in a protoplanetary disk exert torques on a protoplanet at radius R with strength

$$\mathbf{\Gamma} = d\mathbf{J}/dt = \mathbf{R} \times \mathbf{F}. \quad (7)$$

The sum of gravitational forces from all turbulent density perturbations is

$$\mathbf{F} = \sum_i \frac{G\rho_i\Delta V}{r_i^2} \hat{\mathbf{r}}_i, \quad (8)$$

where \mathbf{r}_i is the distance to each gas zone with density ρ_i , $\Delta V = \Delta x \Delta y \Delta z$ is the zone volume and the sum is taken over all zones in the computational domain. In particular,

orbital migration is caused by a change in angular momentum \mathbf{J} , which for a circular orbit in a spherically symmetric potential is simply J_z . Following Nelson & Papaloizou (2004), we consider only a protoplanet at constant R —the center of our shearing box, and thus $dJ_z/dt = \Gamma_z \propto F_y$. In the following analysis, we consider only the properties of the scalar F_y and thus only track migration on circular orbits. We scale F_y in units of $2\pi G\Sigma$, which is the force per unit mass felt by a particle suspended a small distance above the center of a disk with constant Σ . We sample this quantity every 100 timesteps throughout the calculation. While the timestep is dynamically determined and thus fluctuates over the simulation, it maintains an average value of $\sim 10^{-4}t_{\text{orb}}$ with an RMS at least an order of magnitude smaller, giving a sampling rate of roughly $\Delta t \sim 10^{-2}t_{\text{orb}}$.

Figure 4 shows F_y as a function of time for simulations with varying values of Re_M . The RMS value of the force declines with increasing dead zone size. This decrease occurs because it is the MRI in the active layers that drives the density fluctuations, which are in turn responsible for the azimuthal force. For the remainder of the analysis, we consider only torques for times $t > 25t_{\text{orb}}$ in order to avoid any of the transient features from the onset of the MRI evident in Figure 4. We will refer to the value of F_y as “torque,” although it is formally a force per unit mass.

Two critical assumptions of the Fokker-Planck model for planetary migration of JGM06 are that the turbulent torques have temporal stationarity and finite correlation time. We test each of these assumptions for the torque distribution in our simulations.

4.1. Torque Distribution

In order to determine time stationarity, we need the distribution of torques over various fixed time intervals. We can then ask if the samples in each interval are consistent with being drawn from the same distribution as the other intervals. We separate the torque time series into seven $10t_{\text{orb}}$ blocks from $25 - 100t_{\text{orb}}$. Figure 5 shows that the mean of each interval remains near zero over time, and the RMS remains nearly constant. JGM06 require that the torque distribution be such that $\overline{\delta\Gamma(t, J)^2}$ has no time dependence, and this plot demonstrates this for our study. However, the means over each $10t_{\text{orb}}$ bin vary about zero with amplitudes a factor of $\lesssim 0.2$ times the standard deviation over the entire $75t_{\text{orb}}$ sample, suggesting that the underlying distribution of torques does vary slightly over this short an interval. This does not affect the stochastic migration presented here, as such an interval is much shorter than a typical diffusion time in the JGM model.

Additionally, we are interested in the particular distribution of these torques: the central

limit theorem assures us that the cumulative effect of any random process limits to a Gaussian distribution, but can we expect to have a coherent Gaussian over a given (short) period, given the unknown distribution of turbulent forces? Figure 6 shows the distributions of torque over 10 orbit periods for each of the dead zone widths. Each period represents $\sim 10^4$ samples. There is a significant change in the distribution for the $Re_M = 3$ case, although it is consistent with the trend of decreasing standard deviation with decreasing Re_M . Qualitatively, even over such short periods, the torques appear Gaussian distributed, in the sense that they are centrally concentrated on zero and roughly symmetric (figure 6). We quantify this by computing the skew

$$S = \frac{1}{N} \sum_{j=1}^N \left[\frac{x_j - \bar{x}}{\sigma} \right]^3, \quad (9)$$

and kurtosis

$$K = \frac{1}{N} \sum_{j=1}^N \left[\frac{x_j - \bar{x}}{\sigma} \right]^4 - 3, \quad (10)$$

where σ is the standard deviation of the N samples, given in tables 2 and 3 respectively. A normal distribution has skew and kurtosis both equal to zero, while an exponential distribution has kurtosis of three. These tables show that over 10 orbits, the distribution varies from normal significantly—the variance from normal is given using the standard $\sigma_{var} = \sqrt{24/N}$ for kurtosis (Press et al. 1992). This is directly related to the chaotic nature of the MRI: small deviations in initial conditions present at the start of each $10t_{orb}$ block will cause significant deviations (Winters et al. 2003), which we observe as differences in distribution. We note here that this analysis does not affect the JGM assumptions—their model does not require a Gaussian distribution (shown above)—it merely underscores the short-term properties of the MRI.

4.2. Fourier Analysis

Figure 7 shows the temporal power spectra of the torque for runs with varying dead zone widths. Increasing dead zone width has little effect on the shape of the spectrum, changing only the total power. This suggests that the turbulence produces a similar spectrum of density fluctuations, regardless of the width of the dead zone, as we would expect, since the underlying instability is not significantly altered by Ohmic resistivity (Jin 1996; Fleming et al. 2000).

The low frequency power reported by Nelson (2005) is absent in our models, done in the local frame. This suggests that whatever imparts a long-term memory to the turbulence in his simulations is related to the global structure. This conclusion was also noted in

Nelson & Papaloizou (2004) on the basis of running time averages for the migration torque in their local simulations. They find that running averages of the torques tend to zero, while for low mass planets in global simulations, they do not. Our stratified but non-resistive models show a similar convergence, which tends to smaller values at late times for increasing dead zone width (Fig. 8).

As noted in § 4, our time series data is not evenly spaced in time. To correct for this, we interpolate to an even time grid for Fourier analysis. While this can be dangerous for astronomical time series with large gaps (eg., Scargle 1982), we have confirmed that in our case, interpolation is essentially identical to a Lomb Normalized Periodogram (Press et al. 1992), which produces power spectra (but not correlations) for unevenly sampled time series data.

The existence of discrete peaks in the power spectrum indicates the presence of characteristic timescales for the torquing of the protoplanet by MRI turbulence. A more direct measure of this timescale can be found with the autocorrelation function, which we calculate by taking the inverse Fourier transform of the power spectrum. Figure 9 shows autocorrelation functions for each of the medium resolution runs. There is almost no correlation for lags longer than about a dynamical time. Thus, in a local frame at least, turbulent torques are correlated only for a short time, typically $\sim 0.3t_{\text{orb}}$ (see Table 1).

4.3. Locality

It is interesting to understand where the forces relevant to turbulent migration come from. Are they dominated by local forces, or do increasingly large perturbations from large scale motions dominate the total force? Figure 10 shows the total instantaneous force contributed by concentric spherical shells centered on the protoplanet at the box center, calculated as $\Delta F_y(r) = \sum_i F_y(x_i, y_i, z_i)$, for $r^2 < x_i^2 + y_i^2 + z_i^2 < (r + dr)^2$, at four random times for each model. All panels show a sharp drop-off outside of $r \simeq H$, validating the local approach and demonstrating that nearby perturbations tend to dominate over larger turbulent structures.

However, the shearing box imposes a cutoff on the outer scale of MRI turbulence that precludes very large eddies from forming. In particular, at scales large enough for the disk to act as a two-dimensional flow, eddy formation may occur from the inverse cascade of energy expected in two-dimensional flows. We cannot rule out the possibility that such structures may affect protoplanetary migration. JGM06 argue that large eddies will dominate the diffusion coefficient in a turbulent flow because they have longer correlation times. Our

simulations do not address this, as we do not have information about the correlation time as a function of scale. However, we have run a model with twice the radial (x) extent that shows a similar drop-off at a scale of H ensuring that our result is not simply a numerical effect of the small radial size of our box. In addition, we have some insight from the observation that the correlation times differ very little through the sequence of increasing dead zone sizes (see § 4.2). This suggests that the total effect of the various size density structures does not change, even as the various eddy sizes change as a result of the dead zone. Future work will address this point.

Overdensities at the midplane dominate the torque not only in the fully ionized model, but even in models with large dead zones, for two reasons: obviously, they are closer to the protoplanet, and secondly, less obviously, the higher total density at the midplane means that even small perturbations there produce absolute overdensities higher than in the turbulent active layers. Figure 11 shows images of the turbulent overdensities, $\rho - \rho_0(z)$ at $t = 100t_{\text{orb}}$ for all values of Re_M . Subtracting off the initial exponential profile $\rho_0(z)$ simply removes the large symmetric component due to the unperturbed density distribution, allowing the density fluctuations that contribute to the torque to be more easily visualized. The scale bars show the general decline in density perturbation amplitude. Two features are worth noting: the increasing dominance of wave-like structures in these torque images, and the fact that the torque drop-off does *not* come from the MRI moving further away from the planet. While that does happen, the strongest density perturbations remain near the midplane, regardless of the presence of the MRI at that location. The decrease in torque strength for lower magnetic Reynolds numbers is due to the overall lessening of turbulent energy because of both thinner active layers, and reduced energy at saturation due to the higher Ohmic resistivity present even in the active layers. For our ideal MHD runs, $\delta\rho$ is consistent with the relation

$$\frac{\langle \delta\rho^2 \rangle^{0.5}}{\langle \rho \rangle} \simeq \frac{\langle \delta P_{\text{mag}}^2 \rangle^{0.5}}{\langle P \rangle} \quad (11)$$

(Sano et al. 2004), suggesting that their result also applies to stratified disks. For our isothermal runs, $\langle P \rangle = \langle c_s^2 \rho \rangle = c_s^2 \langle \rho \rangle$ and the relation reduces to $\langle \delta\rho^2 \rangle^{0.5} \simeq \langle \delta P_{\text{mag}}^2 \rangle^{0.5} / c_s^2$. Table 4 shows the relationship between volume averaged density and magnetic pressure perturbations for our medium resolution models. As the dead zone size increases so too do the density perturbations relative to the variance of magnetic pressure. This is consistent with the observation of density waves in the dead zone: the active zones drive density perturbations in regions with negligible magnetic pressure, and so volume averages should show just such a trend to higher ratios of the two quantities.

The wave-like structures that we see in the simulations may be the low- m spiral density waves reported in earlier shearing box studies (Hawley, Gammie, & Balbus 1996). The wave

pattern appears similar in all cases because it is driven by the MRI. We switched off the Lorentz force in one of our $Re_M = 30$ simulations, and allowed the evolution to continue for about 6 orbits. With no MRI driving in the active layers, the turbulence quickly dissipates. However, during the decay, the wave pattern remains, although its amplitude drops by roughly a factor of 8 in those 6 orbits. This suggests that the wave pattern may be a natural resonant state of either real disks or merely the shearing box. Although the images reveal wave-like structure, the temporal power spectra of torque do not differ significantly between fully turbulent and dead zone models. Simulations of stochastic excitation of solar p -modes (Nordlund & Stein 2001; Stein & Nordlund 2001) tend to show strong temporal signatures of the excited waves, while our power spectra do not show any obvious wave signatures. We will investigate these structures further in future work.

4.4. Parameterization for Stochastic Models

One of our objectives in this work is to provide parameters necessary for refining the statistical treatment of migration by JGM06 and to understand the predictions it makes when we include dead zones. The extreme computational cost of three-dimensional MHD simulations ensures that the fully global simulation including several scale heights and a few tens of AU in radius evolved to the $\sim 10^5 t_{\text{orb}}$ required to follow planetary migration directly is unlikely in the foreseeable future. Thus, a promising tool in the study of planetary migration is a stochastic method in which one considers the fates of a population of planets subject to random torques from the disk turbulence. JGM06 have constructed an advection-diffusion equation from the Fokker-Planck equation in which standard Type I migration is modeled as advection and turbulent torques are modeled as diffusion (note the important correction in the erratum). Understanding the long term evolution of a population of planets in this model requires a measurement of the diffusion coefficient due to turbulent torques in regions of disks with varying resistivity profiles.

JGM06 derive this diffusion coefficient in terms of the independent variable J , the orbital angular momentum of a protoplanet at a given radius r_p , rather than the radius itself. From a standard Fokker-Planck derivation, JGM06 define the diffusion coefficient as

$$D(J) \equiv \int_{-\infty}^{\infty} \overline{\delta\Gamma(t - \tau/2, J)\delta\Gamma(t + \tau/2, J)} d\tau \simeq \overline{\delta\Gamma(t, J)^2} \tau_c, \quad (12)$$

where τ_c is the correlation time, estimated here from the autocorrelation function (§ 4.2), and the overbars represent ensemble averages. Direct calculation of the integral from our time series for $F_y \propto \Gamma(t, J)$ does not yield satisfactory results, probably because each simulation is only one realization of the torque fluctuations, and $D(J)$ is well-defined only for an ensemble

of such realizations. In lieu of direct calculation, we make use of the rough equivalence $D(J) \simeq \langle \delta\Gamma(t, J)^2 \rangle_t \tau_c$, where we have substituted a time average for the ensemble average in the original.

JGM06 collect all the uncertain properties of turbulence that need to be derived from a numerical model into a single parameter

$$\epsilon = \frac{\tau_c}{t_{\text{orb}}} \left(\frac{C_D}{0.046} \right)^2 = \frac{D}{(0.046)^2 r_p M_p}, \quad (13)$$

where the dimensionless coefficient

$$C_D = \frac{\langle \delta\Gamma^2 \rangle_t^{1/2}}{2\pi G \Sigma r_p M_p}. \quad (14)$$

We calculate C_D using our simulated values of F_y , assuming fixed r_p , and allowing r_p and M_p to cancel between $\delta\Gamma \propto r_p M_p F_y$ and the denominator. Figure 12 shows ϵ as a function of dead zone size in our various simulations. We assume that the ratio of surface densities Σ_D/Σ_A mainly determines the strength of fluctuations in F_y . This facilitates a comparison with the sizes of dead zones predicted by ionization models (e.g. Sano et al. 2000; Fromang et al. 2002; Ilgner & Nelson 2006).

Figure 12 includes a resolution study. The circled values show the same model at all three different resolutions, while the two sets of models with extreme values of Re_M were run at the lower two resolutions. (Remember that the same value of Re_M produces different dead zone thicknesses at different resolutions, as shown in Figure 3(a).) All of these comparisons show that our derived diffusion parameter ϵ drops steadily with increasing resolution, suggesting it is less well converged than the average torque or dead zone thickness (Fig. 3(a)). Thus, our estimates of the diffusion coefficient and related quantities appear likely to be firm upper limits to the true values.

JGM06 derive a fiducial value of $\epsilon \sim 0.5$ from the ideal MHD simulations of Nelson (2005). Our local ideal MHD simulation, on the other hand, gives a value of $\epsilon \simeq 10^{-3}$ at medium resolution. On the other hand, JGM06 derive a fiducial correlation time of ~ 0.5 from Nelson’s simulations, which is quite close to our ~ 0.3 value. This suggests that it is differences in the torque magnitudes, rather than correlation times, that drives the difference. The torque magnitudes are driven directly by the MRI perturbations, which in turn may differ from N05 due to his lack of stratification, by the difference in MRI strengths (his models have $\alpha \simeq 5 \times 10^{-3}$, larger than ours by a factor of a few), or by a difference in density perturbations between global and local models. In our models with dead zones, we find $10^{-5} \lesssim \epsilon \lesssim 10^{-3}$ over $3 \leq Re_M \leq \infty$.

In the disk model that we employ, even our ideal MHD model gives a value of ϵ that suggests a terrestrial-mass planet in even our most turbulent model will be in the advection dominated regime, as shown in Figure 7 of JGM06. (Note that the flat parts of the curve in that Figure correspond to advection.) However, even this reduced value of ϵ is sufficient to drive diffusive migration for protoplanets in the sub-Earth mass range. For such planets, dead zones may shift migration from diffusion to advection as they pass radially in from a fully active region with stronger turbulence.

4.5. Dead Zone Sizes

Given the decrease of $\epsilon(J)$ with increasing dead zone size that we find at all resolutions, it is reasonable to ask how close our models come to a realistic dead zone thickness. Previous studies of the ionization fraction in disks robustly show that the presence of small dust grains ($< 1 \mu\text{m}$) with interstellar abundance will cause dead zones to be orders of magnitude larger in column density than their active zones (Sano et al. 2000; Semenov et al. 2004; Ilgner & Nelson 2006). Our $Re_M = 3$ models only reach a surface density ratio $\Sigma_D/\Sigma_A \simeq 10$, making dynamical models with significant submicron dust grains well outside of current computational limits. However, once these dust grains either sediment to the disk midplane or coagulate, ionization occurs much more rapidly and the dead zone size shrinks. This may occur in a small fraction of the disk lifetime, although a population of new small grains with different properties could then be produced by collisional processes (Dullemond & Dominik 2005). For an α -disk with $\dot{M} = 10^{-7} M_\odot/\text{yr}$ and $\alpha = 10^{-2}$, the surface density ratios become $\Sigma_D/\Sigma_A = 9.1$ at 1 AU and 1.1 at 5 AU (Ilgner & Nelson 2006). While this model assumes an α -value somewhat greater than we find, it suggests that simulations such as ours may not be so far from realistic dead zone sizes. Our results indicate that this ratio influences the magnitude of turbulent torques and thus could determine the transition between advection- and diffusion-dominated migration regimes for a variety of protoplanetary masses.

5. Discussion

Our results indicate that in the thick dead zone that is expected around 1–5 AU, turbulent torques will be reduced by at least two orders of magnitude from those expected in a fully turbulent disk at the same radii, allowing a uniform inward Type I migration mode to become dominant even for protoplanets with $M_p \ll M_\oplus$. A potential consequence of this is that if such protoplanets form further out in the disk where the dead zone is thinner, the inner, thick dead zone region of the disk could act as a sink for protoplanets following

random walks driven by the more vigorous turbulence expected further out.

Because our simulations are local, we can only provide $\delta\Gamma(t, J)$ at one value of angular momentum J (that is, one radial location in the disk). A radial gradient of the diffusion coefficient $D(J)$ contributes to *advection* and does not affect our main results on dead zone diffusive migration. Indeed, a strong gradient in the diffusion coefficient might be present at the radial boundary between an active and dead zone in the midplane. Most models of protoplanetary disk ionization suggest that there will be two such boundaries, one in the outer disk where the column density increases to the point that protostellar X-rays can no longer penetrate to the midplane, and one in the inner disk where thermal ionization begins to become important. JGM06 note that the orbital flux F_J of the planet distribution function f can be written as

$$F_J = (\bar{\Gamma} - \partial_J D)f - D\partial_J f, \quad (15)$$

emphasizing the contribution of $\partial_J D$ to the effective mean migration. In a region where protoplanets cross from an active region to a dead zone in the midplane, ϵ , and thus D (eq. 13) changes by several orders of magnitude (Fig. 12) over a region of uncertain but likely sub-AU width. At the inner boundary of the dead zone, $\partial_J D < 0$ contributing to outward mean migration, while at the outer boundary, $\partial_J D > 0$, contributing to inward mean migration. Thus, the random walk migration induced by a fully turbulent disk tends to make the dead zone act as a trap for sub-terrestrial mass protoplanets.

The magnitude of this effect is difficult to estimate from our simulations because we ignore background gradients in the disk, and thus our measurements of dead zone and fully active turbulent torques are at equivalent radial positions in the disk. Nonetheless, future global and statistical models should be able to predict if the effect overcomes Type I migration in these regions strongly enough for the dead zone to function as an efficient trap.

Recently, Turner, Sano, & Dziourkevitch (2006) have performed simulations including a dynamic $\eta(x, y, z, t)$ in which the dead zone disappears, at least from the point of view of angular momentum transport: their results suggest that while the MRI remains suppressed below $|z| \sim 0.5H$, there is still significant Maxwell stress from mean fields that build up due to the vertical expulsion of flux and the regeneration of azimuthal field from shear. They suggest that these fields may grow large enough to invoke the Terquem (2003) migration mechanism in which magnetic resonances close to the planet may reverse Type I migration. However, these results—while provocative—should not significantly alter our main results. In our case, we isolate the turbulent contribution to migration, ignoring the gravitational back-reaction of a protoplanet on the disk. Any effects of the midplane mean field, such as the Terquem (2003) mechanism, are therefore absent by construction. Indeed, since the MRI is suppressed at the midplane in the Turner et al. (2006) simulations, the turbulent

overdensities will be reduced, as in our simulations.

Our work depends on two major approximations: the restriction of our simulation to the local, shearing box, and the adaptation of zero-mass test particles fixed at the center of the box. Because of the latter assumption, the possibility exists that our results underestimate correlations because a moving particle would accelerate in the direction of the largest current density fluctuation, thus increasing the torque. However, the density structures will still have lifetimes on the order of an orbit and they will not have different spatial distributions. This means that in the lifetime of the fluctuation, the protoplanet will not have time to move significantly from its current position. Estimating the distance by an impulse approximation, the distance moved over the lifetime of a perturbation is roughly $x/H \sim 10^{-6}$ —a trivial amount. Any global dynamical structures associated with the MRI are absent from our models, including large scale eddies that could change our results if they are sufficiently massive. Large scale dynamical features may also affect the correlation times of torques. Despite these caveats, we generally expect our results to be qualitatively valid in demonstrating that dead zones are regions of significantly reduced diffusive migration. Dead zones may also have other consequences for planetary migration such as those considered by Matsumura & Pudritz (2003) and Matsumura et al. (2007).

6. Conclusions

We find that a dead zone in a protoplanetary disk can reduce the magnitude of turbulent torque fluctuations on migrating protoplanets by at least two orders of magnitude from a comparable fully ionized region. The thick dead zone expected at 1 AU, assuming a dust-depleted disk, can have significant consequences for migration of planets with $M_p \ll M_\oplus$ driven by turbulent density fluctuations.

The central assumptions of the stochastic diffusion model of protoplanetary migration of JGM06 amenable to test in local simulations seem well-founded. The torques have a finite correlation time and have stationary distributions. These fluctuations maintain nearly constant correlation times, independent of their amplitude. The stochastic diffusion model suggests that if protoplanets form outside of the dead zone and migrate in a diffusive manner, the dead zone may act as a sink.

JSO would like to thank the Max-Planck-Institut für Astronomie for its kind hospitality during a portion of this work, during which he was supported by an Annette Kade Graduate Student Fellowship. M.K.R. Joungh and R. Nelson made numerous helpful suggestions for which we thank them. This work was partly supported by the NASA Origins of Solar Systems

Program under grant number NNX07AI74G, as well as by the NSF under grant number AST-0307793. Computations were performed on the Beehive Cluster at Columbia University, the Parallel Computing Facility at AMNH, the Cray XT3 “Big Ben” at the Pittsburgh Supercomputing Center, and the IBM SP “Datastar” at the San Diego Supercomputing Center. The last two are supported by the National Science Foundation.

REFERENCES

- Balbus, S. A., & Hawley, J. F. 1998, *Rev. Mod. Phys.*, 70, 1
- Butler, R. P., et al. 2006, *ApJ*, 646, 505
- Brandenburg, A., Nordlund, Å., Stein, R. F., & Torkelsson, U. 1995, *ApJ*, 446, 741
- Brandenburg, A. 1998, in *Theory of Black Hole Accretion Disks*, eds. M. A. Abramowicz, G. Bjornsson, & J. E. Pringle (Cambridge: Cambridge U. Press) 61
- Brandenburg, A., & Dobler, W. 2002, *Comput. Phys. Comm.*, 147, 471
- Brandenburg, A., Dintrans, B., & Haugen, N. E. L. 2004, in *AIP Conf. Proc. 733: MHD Couette Flows: Experiments and Models*, 733, 122
- D’Angelo, G., Kley, W., & Henning, T. 2003, *ApJ*, 586, 540
- D’Angelo, G., Bate, M. R., & Lubow, S. H. 2005, *MNRAS*, 358, 316
- Dullemond, C. P., & Dominik, C. 2005, *A&A*, 434, 971
- Fleming, T. P., Stone, J. M., & Hawley, J. F. 2000, *ApJ*, 530, 464
- Fleming, T., & Stone, J. M. 2003, *ApJ*, 585, 908
- Fromang, S., Terquem, C., & Balbus, S. A. 2002, *MNRAS*, 329, 18
- Fromang, S., & Nelson, R. P. 2006, *A&A*, 457, 343
- Fromang, S., & Papaloizou, J. 2007, *A&A submitted* (astro-ph:0705.3621)
- Gammie, C. F. 1996, *ApJ*, 457, 355
- Goldreich, P., & Lynden-Bell, D. 1965, *MNRAS*, 130, 125
- Goldreich, P., & Tremaine, S. 1980, *ApJ*, 241, 425

- Gould, A., Dorsher, S., Gaudi, B. S., & Udalski, A. 2006, *Acta Astron.*, 56, 1
- Hartmann, L., Calvet, N., Gullbring, E., & D'Alessio, P. 1998, *ApJ*, 495, 385
- Haugen, N. E. L., Brandenburg, A., & Mee, A. J. 2004, *MNRAS*, 353, 947
- Hawley, J. F., Gammie, C. F., & Balbus, S. A. 1995, *ApJ*, 440, 742
- Hawley, J. F., Gammie, C. F., & Balbus, S. A. 1996, *ApJ*, 464, 690
- Hubickyj, O., Bodenheimer, P., & Lissauer, J. J. 2005, *Icarus*, 179, 415
- Ilgner, M., & Nelson, R. P. 2006, *A&A*, 445, 205
- Jang-Condell, H., & Sasselov, D. D. 2005, *ApJ*, 619, 1123
- Jayawardhana, R., Coffey, J., Scholz, A., Brandeker, A., & van Kerkwijk, M. H. 2006, *ApJ*, 648, 1206
- Ji, J., Kinoshita, H., Liu, L., & Li, G. 2003, *ApJ*, 585, L139
- Jin, L. 1996, *ApJ*, 457, 798
- Johansen, A., & Klahr, H. 2005, *ApJ*, 634, 1353
- Johnson, E. T., Goodman, J., & Menou, K. 2006, *ApJ*, 647, 1413 [erratum: 654, 1177]
- Lang, K. R. 1980, *Astrophysical Formulae* (New York: Springer).
- Laughlin, G., Steinacker, A., & Adams, F. C. 2004, *ApJ*, 608, 489
- Lee, M. H., & Peale, S. J. 2002, *ApJ*, 567, 596
- Lee, M. H., Butler, R. P., Fischer, D. A., Marcy, G. W., & Vogt, S. S. 2006, *ApJ*, 641, 1178
- Lin, D. N. C., & Papaloizou, J. 1979, *MNRAS*, 186, 799
- Masset, F. S. 2002, *A&A*, 387, 605
- Masset, F. S., & Papaloizou, J. C. B. 2003, *ApJ*, 588, 494
- Matsumura, S., & Pudritz, R. E. 2003, *ApJ*, 598, 645
- Matsumura, S., Pudritz, R. E., & Thommes, E. W. 2006, *ApJ*, accepted (astro-ph/0606237)
- Menou, K., & Goodman, J. 2004, *ApJ*, 606, 520

- Miyoshi, K., Takeuchi, T., Tanaka, H., & Ida, S. 1999, *ApJ*, 516, 451
- Nelson, R. P. 2005, *A&A*, 443, 1067
- Nelson, R. P., & Papaloizou, J. C. B. 2003, *MNRAS*, 339, 993
- Nelson, R. P., & Papaloizou, J. C. B. 2004, *MNRAS*, 350, 849
- Nordlund, Å., & Stein, R. F. 2001, *ApJ*, 546, 576
- Stein, R. F., & Nordlund, Å. 2001, *ApJ*, 546, 585
- Paardekooper, S.-J., & Mellema, G. 2006, *A&A*, 459, L17
- Papaloizou, J. C. B., & Nelson, R. P. 2003, *MNRAS*, 339, 983
- Papaloizou, J. C. B., Nelson, R. P., & Snellgrove, M. D. 2004, *MNRAS*, 350, 829
- Pollack, J. B., Hubickyj, O., Bodenheimer, P., Lissauer, J. J., Podolak, M., & Greenzweig, Y. 1996, *Icarus*, 124, 62
- Press, W. H., Teukolsky, S. A., Vetterling, W. T., & Flannery, B. P. 1992 *Numerical Recipes* (Cambridge: Cambridge University Press) 2nd ed.
- Rice, W. K. M., & Armitage, P. J. 2003, *ApJ*, 598, L55
- Sano, T., Miyama, S. M., Umebayashi, T., & Nakano, T. 2000, *ApJ*, 543, 486
- Sano, T., & Inutsuka, S.-I. 2001, *ApJ*, 561, L179
- Sano, T., Inutsuka, S.-I., Turner, N. J., & Stone, J. M. 2004, *ApJ*, 605, 321
- Scargle, J. D. 1982, *ApJ*, 263, 835
- Semenov, D., Wiebe, D., & Henning, T. 2004, *A&A*, 417, 93
- Shakura, N. I., & Sunyaev, R. A. 1973, *A&A*, 24, 337
- Stone, J. M. & Norman, M. L. 1992, *ApJS*, 80, 753
- Stone, J. M., Hawley, J. F., Gammie, C. F., & Balbus, S. A. 1996, *ApJ*, 463, 656
- Tanaka, H., Takeuchi, T., & Ward, W. R. 2002, *ApJ*, 565, 1257
- Terquem, C. E. J. M. L. J. 2003, *MNRAS*, 341, 1157
- Turner, N., Sano, T., & Dziourkevitch, N. 2006, *ApJ*, in press (astro-ph/0612552)

Ward, W. R. 1986, *Icarus*, 67, 164

Ward, W. R. 1997, *ApJ*, 482, L211

Weidenschilling, S. J. 1977, *MNRAS*, 180, 57

Winters, W. F., Balbus, S. A., & Hawley, J. F. 2003, *MNRAS*, 340, 519

Table 1. Basic parameters for all runs.

Name	Resolution	Re_M^a	t_{max}/t_{orb}^b	Σ_A/Σ_D^c	$\langle F_y^2 \rangle_t^{0.5d}$	τ_c/t_{orb}^e
32Rinf	32×128^2	∞	100	-	5.17(-3)	0.31
32R100	32×128^2	100	100	1.65	2.63(-3)	0.31
32R30	32×128^2	30	200	1.13	2.27(-3)	0.39
32R3	32×128^2	3	100	0.177	5.17(-4)	0.24
64Rinf	64×256^2	∞	100	-	3.23(-3)	0.31
64R100	64×256^2	100	100	1.37	1.90(-3)	0.43
64R30	64×256^2	30	100	0.860	1.49(-3)	0.29
64R3	64×256^2	3	100	0.102	3.45(-4)	0.33
128R30	128×512^2	30	50	0.660	1.29(-3)	0.25

^aMagnetic Reynolds number

^bSimulation time in orbits

^cSurface density ratio of active to dead zones

^dRMS y-component of force on protoplanet over orbits 25-100

^eTorque correlation time in orbits

Table 2. Skew for 10 orbit intervals from $25 - 95t_{orb}$ for 64×256^2 runs. Columns are labeled by the interval center time in orbits

Re_M	30	40	50	60	70	80	90
∞	-0.283	0.463	0.076	-0.157	0.209	-0.026	0.028
100	0.175	-0.158	-0.505	-0.113	-0.170	-0.651	-0.163
30	-0.240	0.305	0.277	-0.123	0.254	-0.680	0.455
3	0.097	0.278	0.673	0.145	0.048	-0.001	0.076

Table 3. Kurtosis for 10 orbit intervals from $25 - 95t_{orb}$ for 64×256^2 runs. Columns are labeled by the interval center time in orbits.

Re_M	30	40	50	60	70	80	90
∞	0.657	1.446	0.460	0.379	0.555	1.025	1.274
100	0.910	0.304	0.425	0.064	0.675	0.944	0.439
30	2.066	1.133	1.057	0.201	0.573	3.112	1.223
3	0.362	0.746	2.883	0.923	0.921	1.386	0.258

Table 4. Ratios of RMS density fluctuations and magnetic pressure.

Run Name	$\langle \delta \rho^2 \rangle^{0.5}$ ^a	$\langle \delta P_{mag}^2 \rangle^{0.5} / c_s^2$ ^b	$c_s^2 \langle \delta \rho^2 \rangle^{0.5} / \langle \delta P_{mag}^2 \rangle^{0.5}$ ^c
32Rinf	3.80(-2)	1.16(-2)	3.27
32R100	2.51(-2)	5.93(-3)	4.24
32R30	2.80(-2)	2.80(-3)	9.98
32R3	6.84(-3)	3.12(-4)	21.9
64Rinf	4.27(-2)	1.93(-2)	2.22
64R100	2.32(-2)	4.01(-3)	5.78
64R30	1.74(-2)	2.28(-3)	7.63
64R3	7.58(-3)	2.22(-4)	34.2
128R30	1.64(-2)	1.26(-3)	13.0

^aRMS density fluctuations at $t = 50t_{orb}$

^bvariance of magnetic pressure normalized by c_s^2 at $t = 50t_{orb}$

^cratio of cols a and b

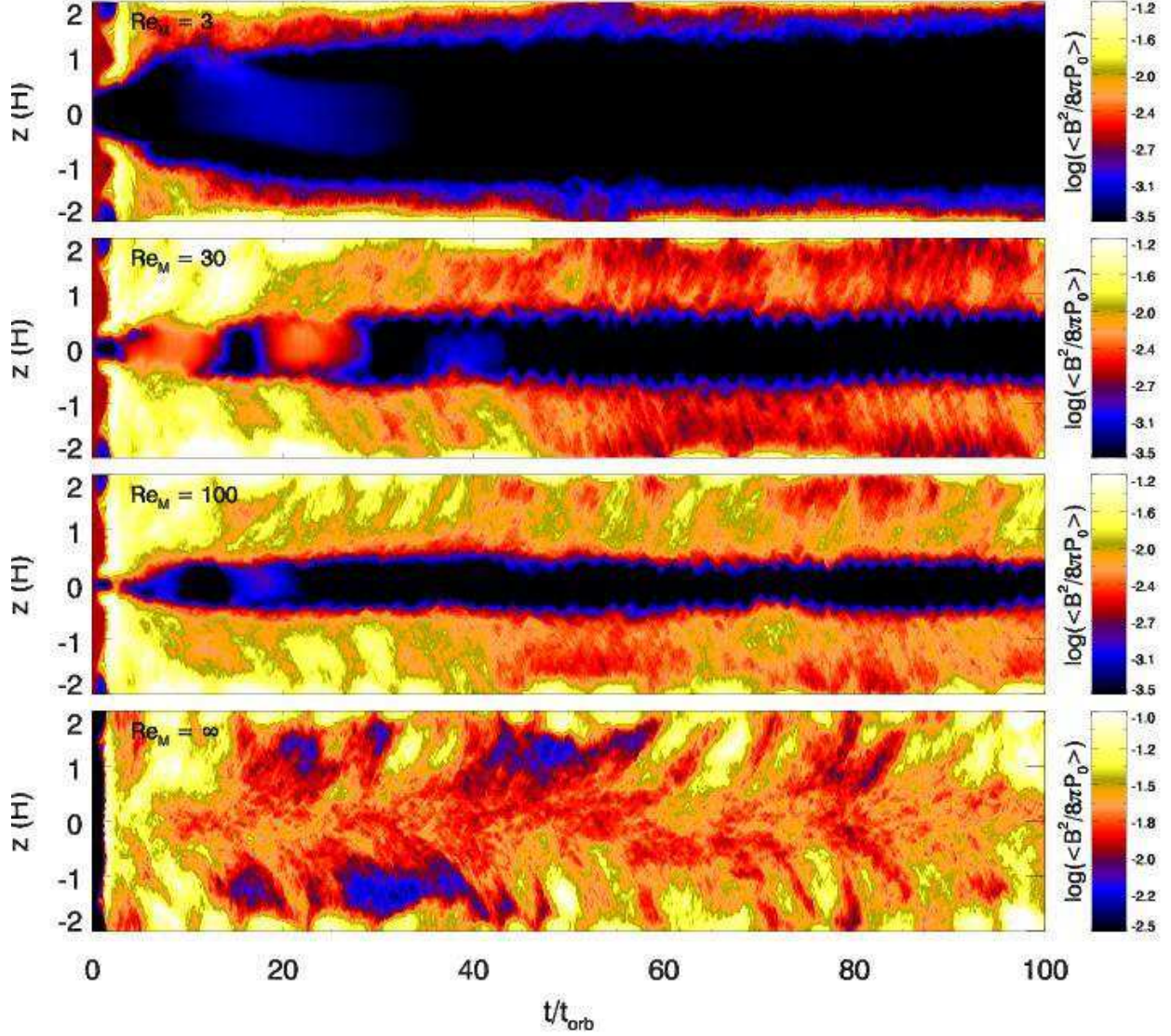


Fig. 1.— Space-time diagrams of magnetic energy averaged over horizontal ($x - y$) planes for runs with (from bottom to top) $Re_M = \infty$, 100, 30, and 3. The dead zone is apparent in all models with finite Re_M . Note that the color scale is shifted to higher values for the bottom panel

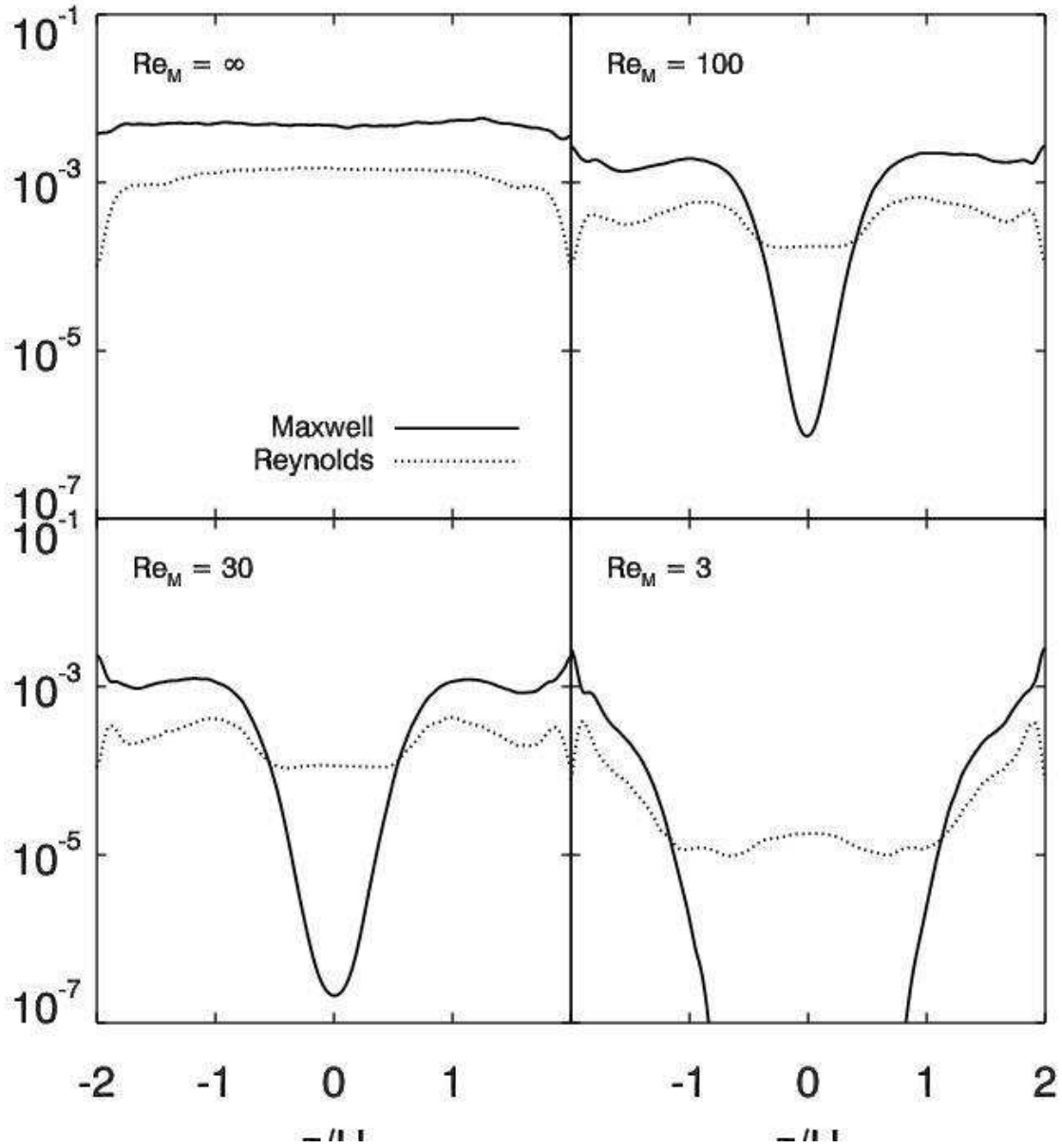


Fig. 2.— Vertical profiles of Reynolds and Maxwell stresses for medium resolution runs with four different values of magnetic Reynolds numbers Re_M . Note that the Reynolds stress remains nearly constant across the dead zone, even as the dead zone depth increases.

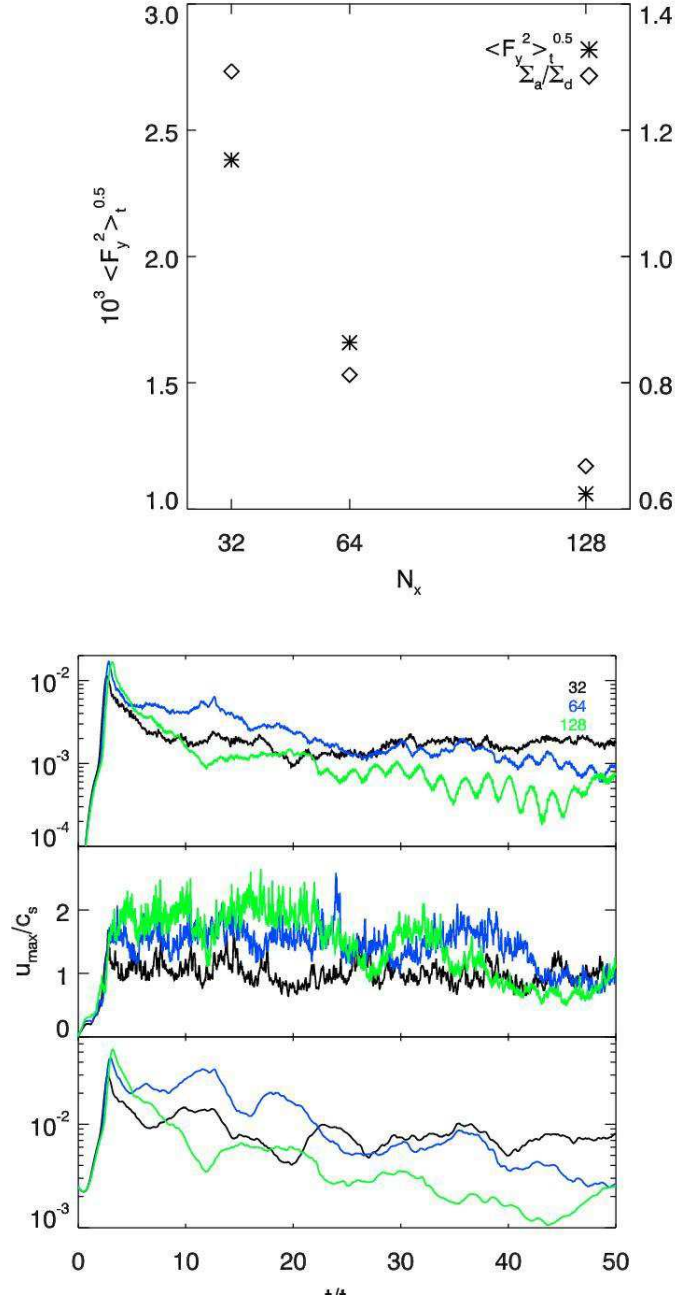


Fig. 3.— A resolution study for a $Re_M = 30$ model. Resolutions corresponding to $dx = 3.125 \times 10^{-2}$, 1.563×10^{-2} , and 7.813×10^{-3} are labeled by $N_x = 32$, 64 , and 128 . Variables shown include (a) the temporal RMS azimuthal gravitational force $\langle F_y^2 \rangle_t^{0.5}$ (stars) and the active-to-dead zone column density ratio Σ_a / Σ_d (diamonds) versus resolution; and (b) volume averages of the effective dimensionless viscosity $\alpha = (\langle \rho u_x u_y \rangle - \langle B_x B_y \rangle) / P_0$ (top), RMS Mach number (middle), and magnetic energy normalized to initial midplane pressure P_0 (bottom), as a function of time in orbital units.

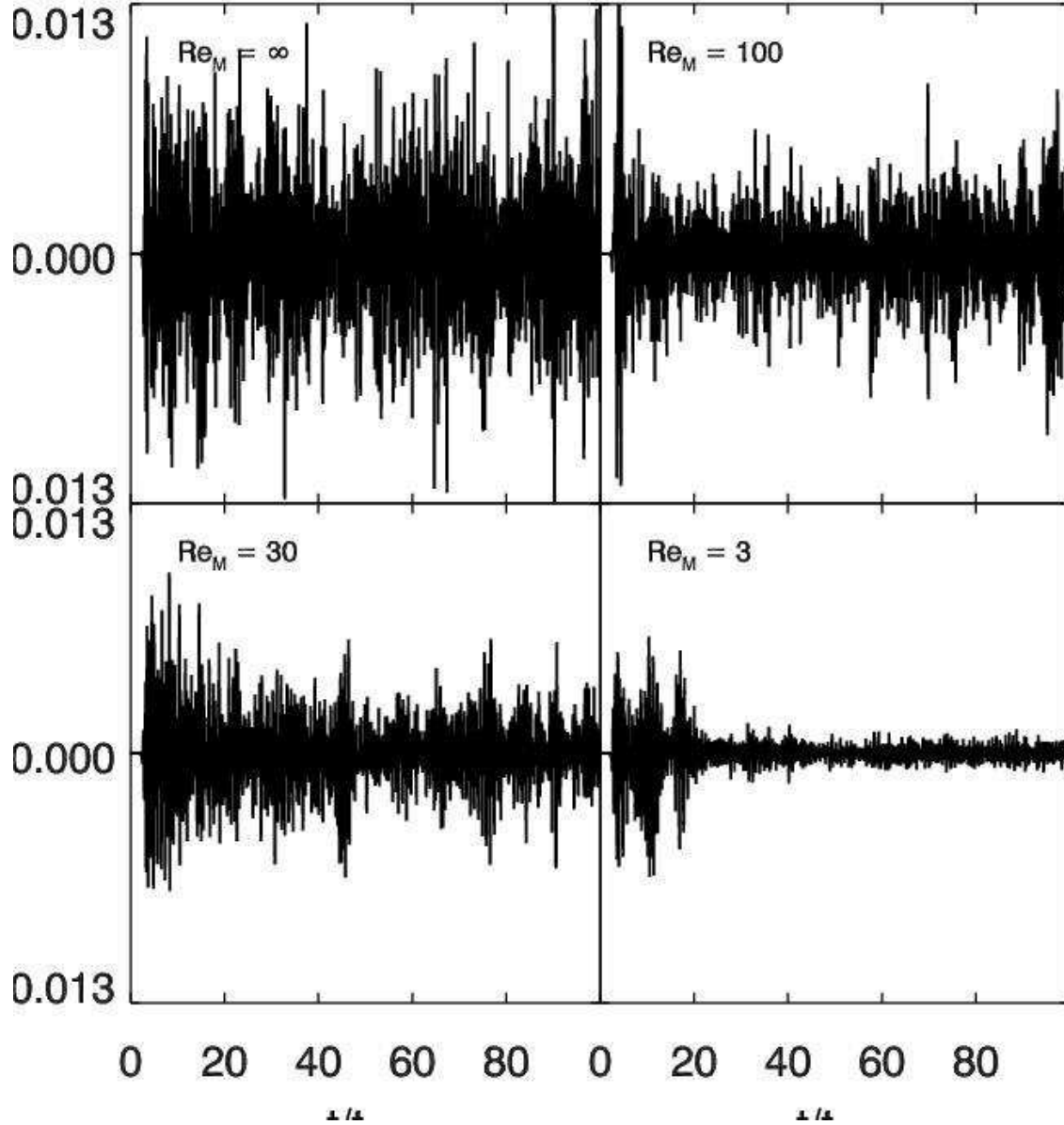


Fig. 4.— Time series of azimuthal gravitational force F_y in 64×256^2 resolution runs. The force is scaled in units of $2\pi G\Sigma$, the vertical restoring force near the midplane.

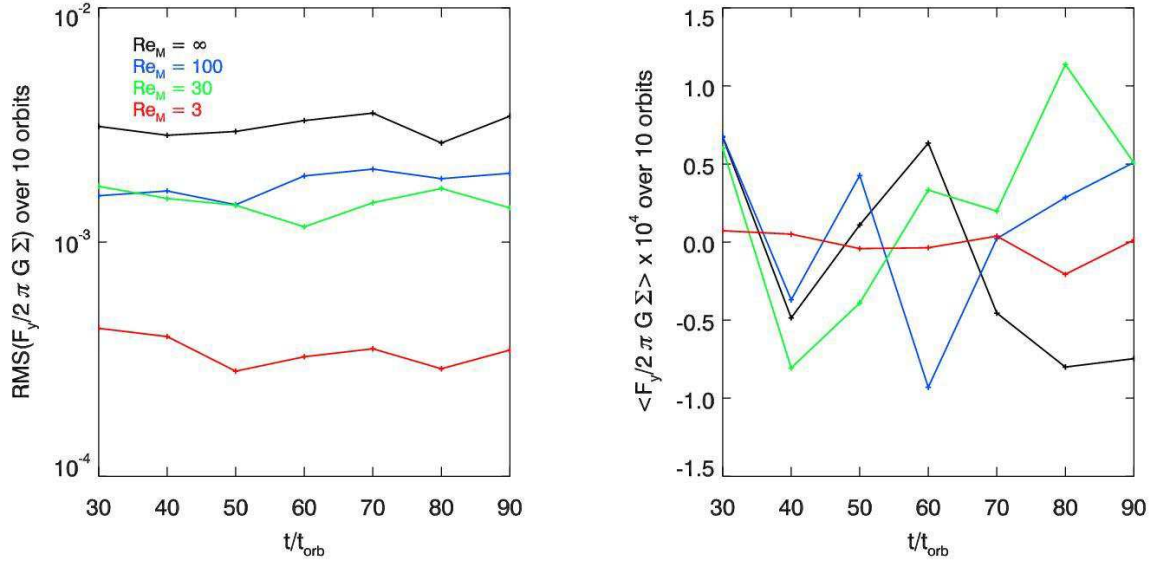


Fig. 5.— RMS (left) and mean values (right) of the torque F_y for seven periods each of length $10t_{\text{orb}}$, labeled by the interval midpoint. The $10t_{\text{orb}}$ means show weak fluctuations around the global time standard deviation, as much as a factor of ~ 0.2 in the $Re_M = 3$ case, and a factor of a few in all cases.

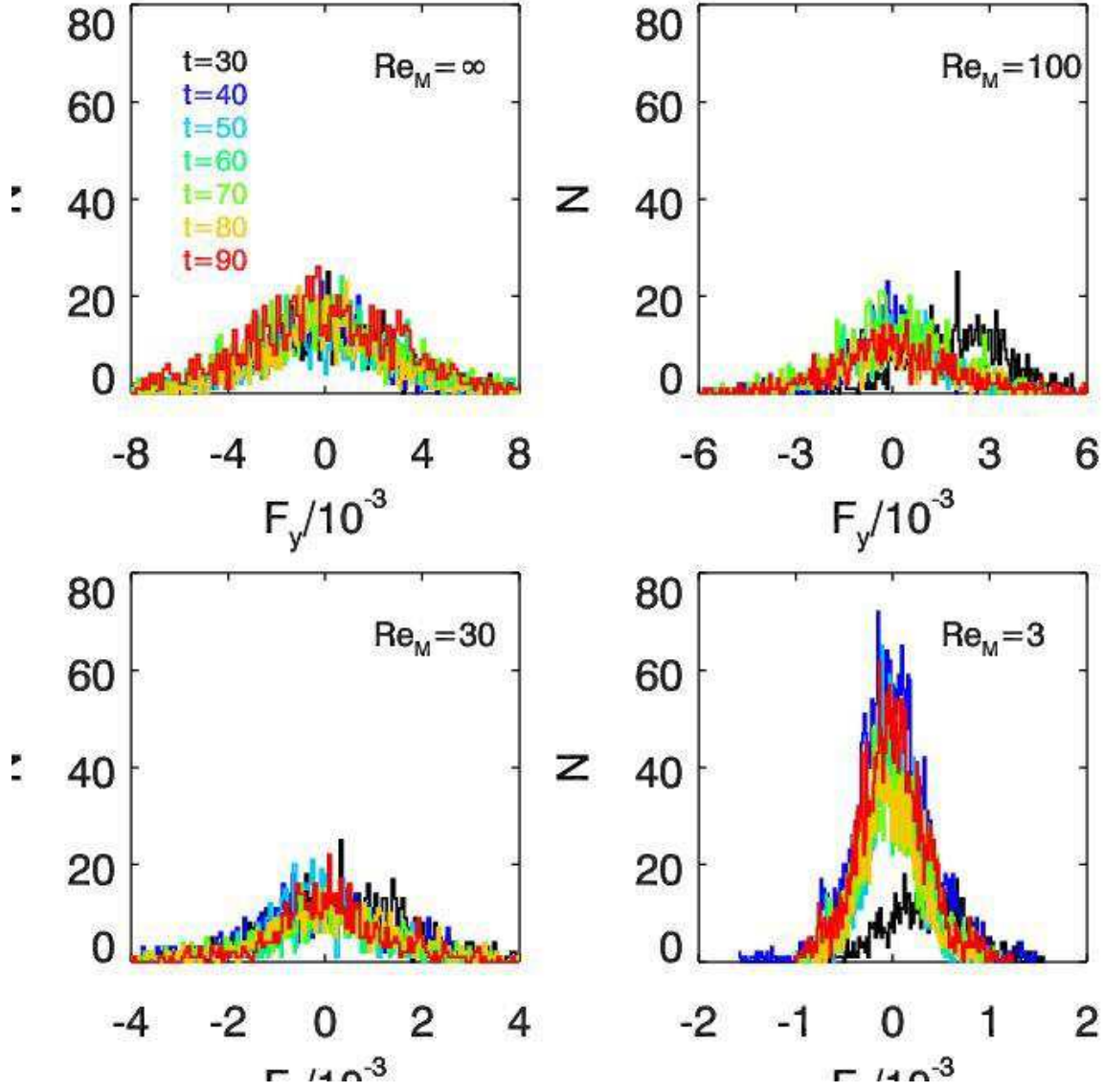


Fig. 6.— Distributions of torque exerted on protoplanets in models with various Re_M . Each panel shows the distributions for seven periods, each of length $10t_{\text{orb}}$ (from $25t_{\text{orb}}$ to $95t_{\text{orb}}$), labeled by the interval midpoint. Note the decreasing range along the x -axis from model to model, indicating a narrower range of torque amplitudes for larger dead zone models. The distributions appear time stationary after the initial 10 orbits.

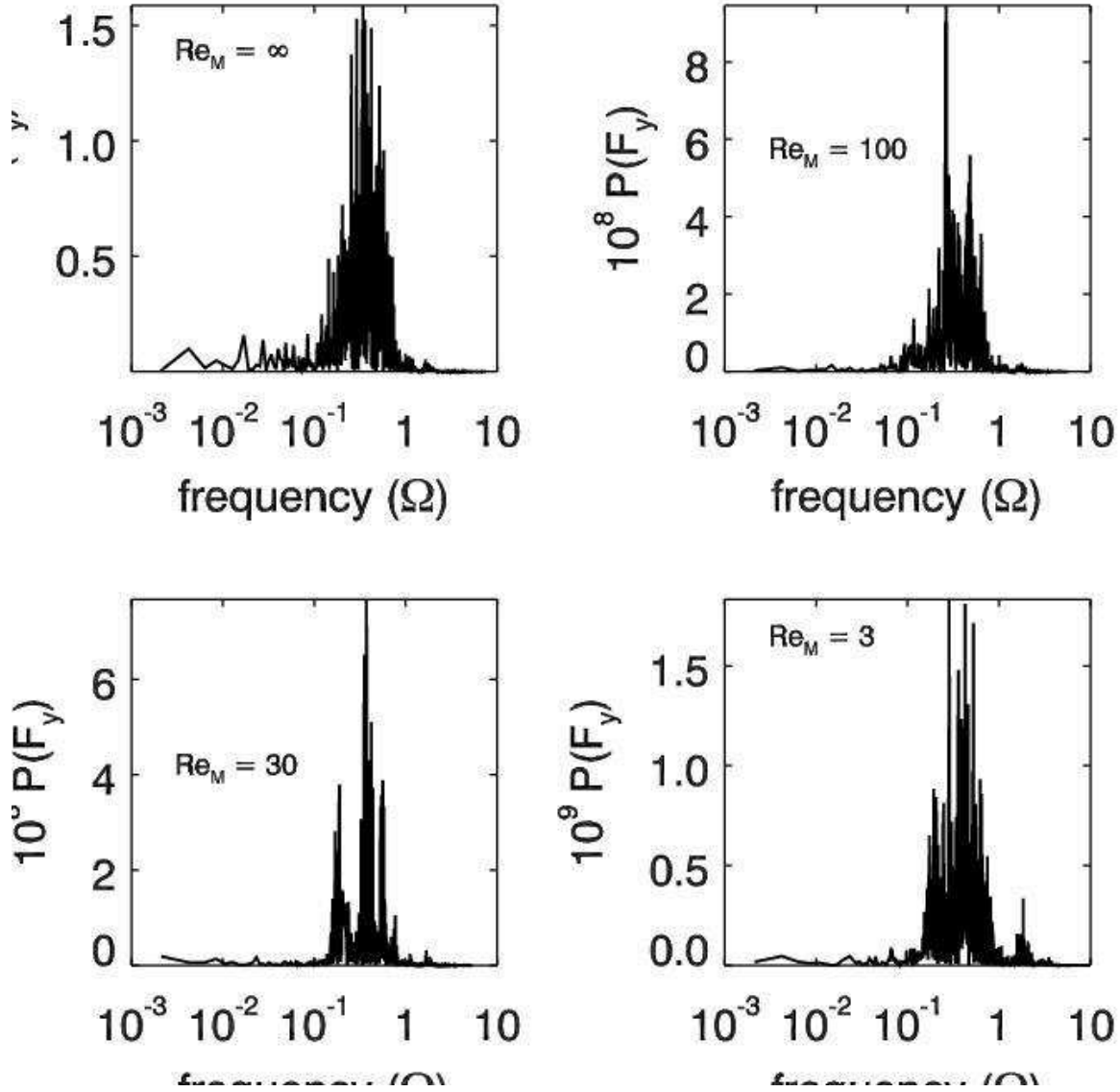


Fig. 7.— Power spectra of torque fluctuations F_y in four medium resolution models with increasing dead zone width. Note the decreasing value of the vertical scale from model to model. Very little power is seen at low frequencies.

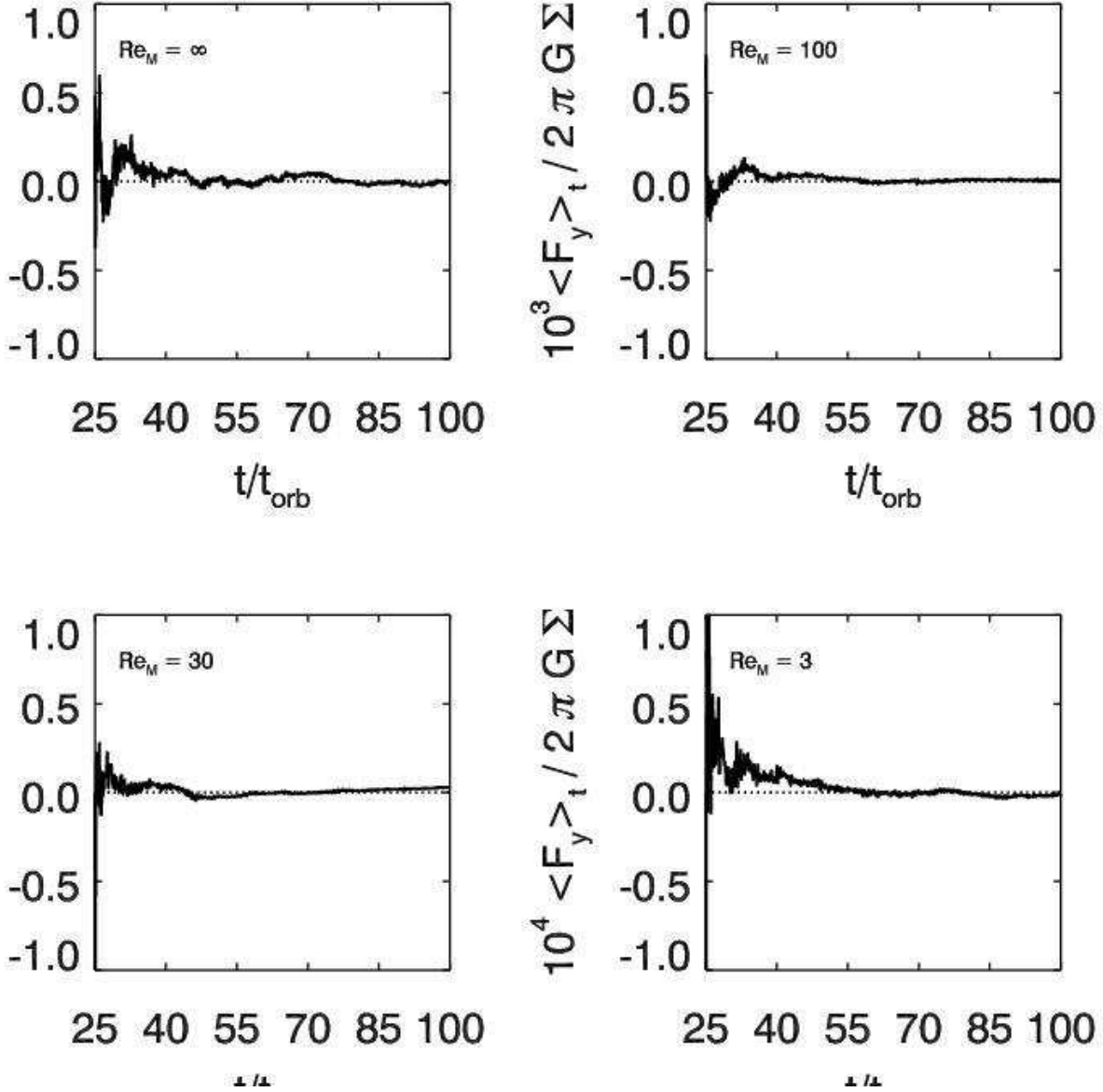


Fig. 8.— Running time average of the torque F_y in the four medium resolution models with increasing dead zone size, starting at $t = 25t_{\text{orb}}$ to eliminate effects of the initial transient. The dotted line marks the zero point. The ordinate is a factor of ten smaller for the $Re_M = 3$ case than for the others. In all cases, the running average approaches zero at late times.

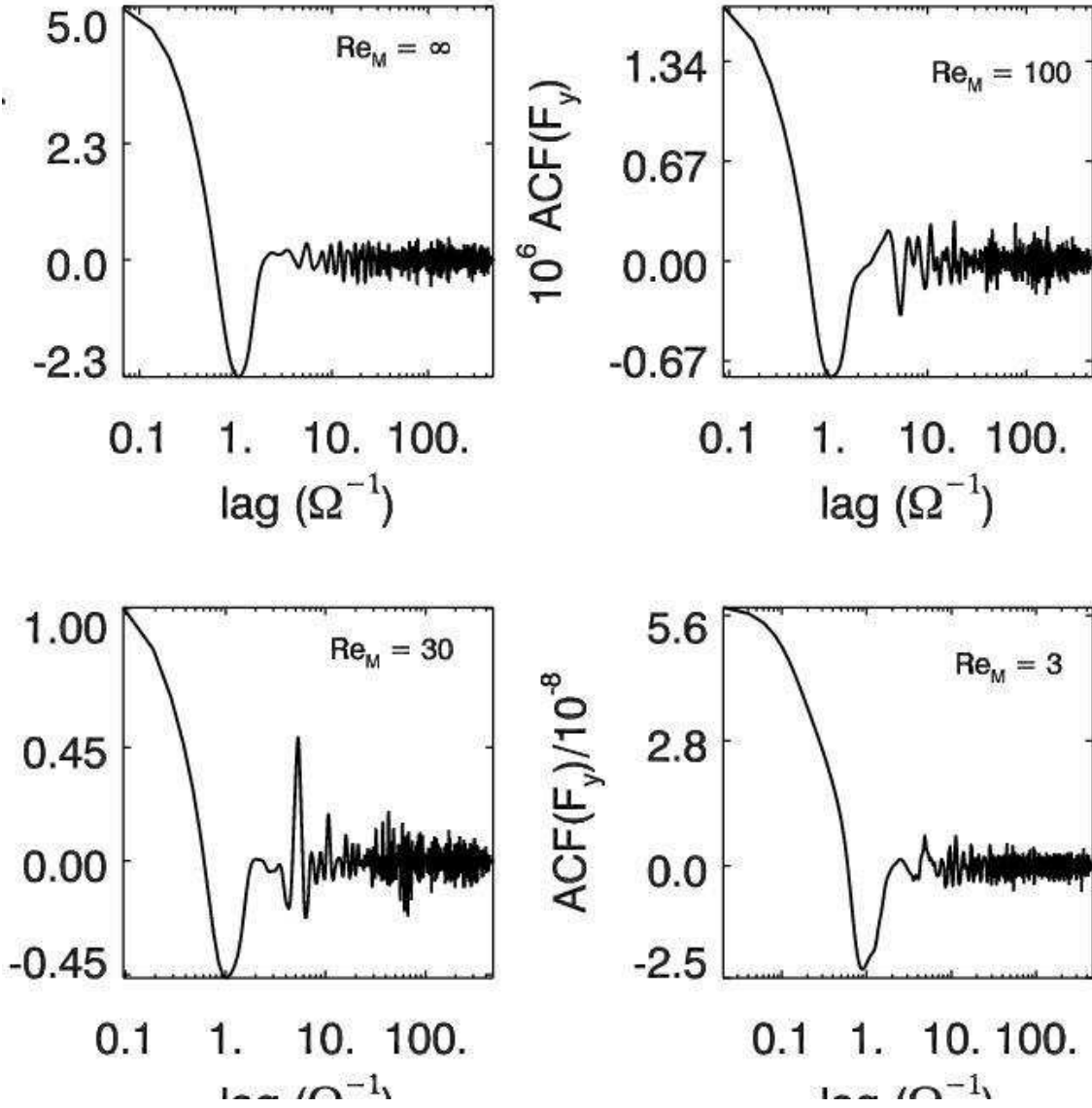


Fig. 9.— Autocorrelation functions of the torque (F_y) fluctuations in the four medium resolution models with increasing dead zone width. All models have similar correlation times, roughly defined as the point where the curve first crosses zero with positive first derivative.

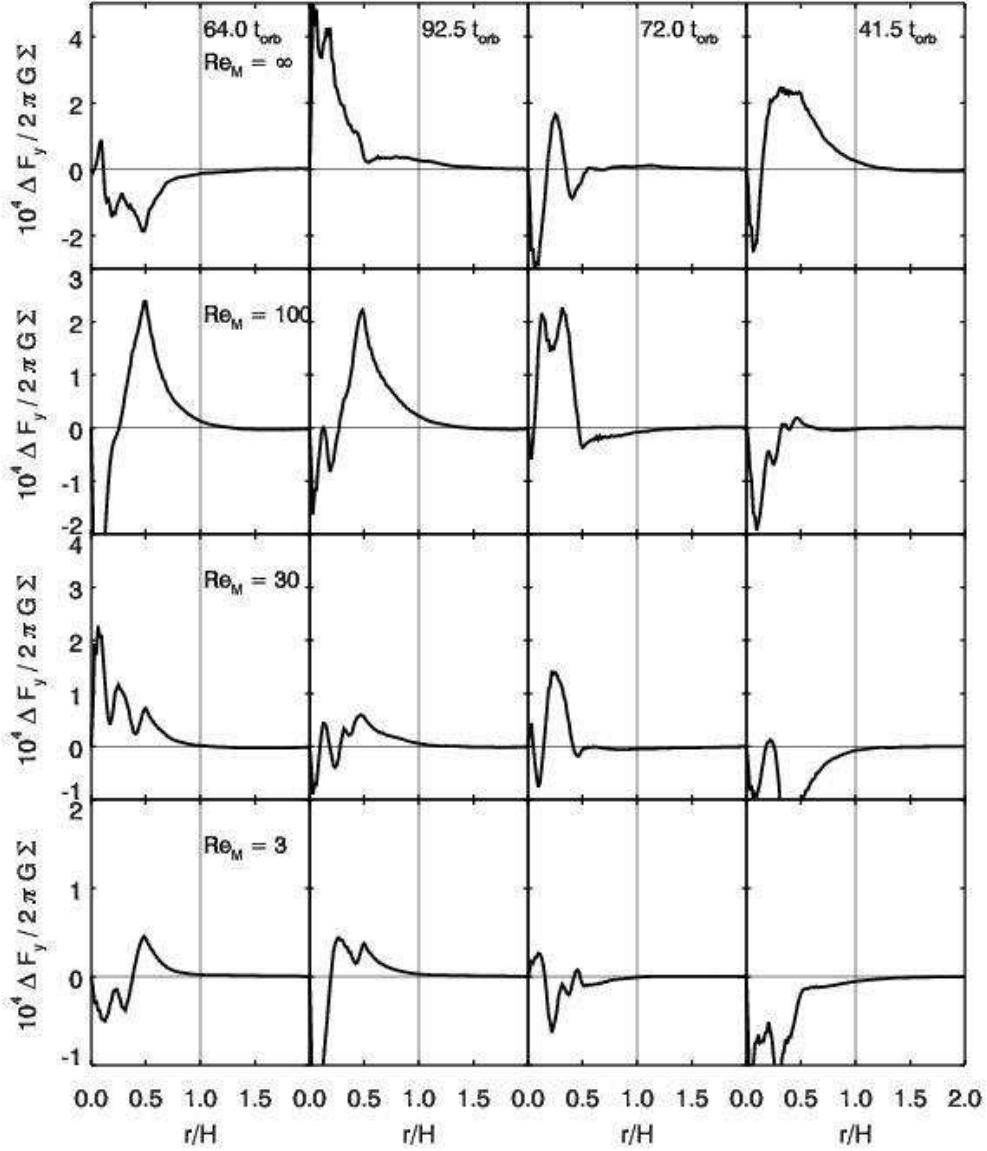


Fig. 10.— Cumulative torque contributions δF_y from spherical shells as a function of radial distance r from the box center shown at four random times in medium resolution models with increasing dead zone size (from top to bottom, $Re_M = \infty, 100, 30, 3$). In all models, the torque vanishes at or near $r \sim H$, the disk scale height. The thin lines mark the zero point on the ordinate and $r = H$ on the abscissa.

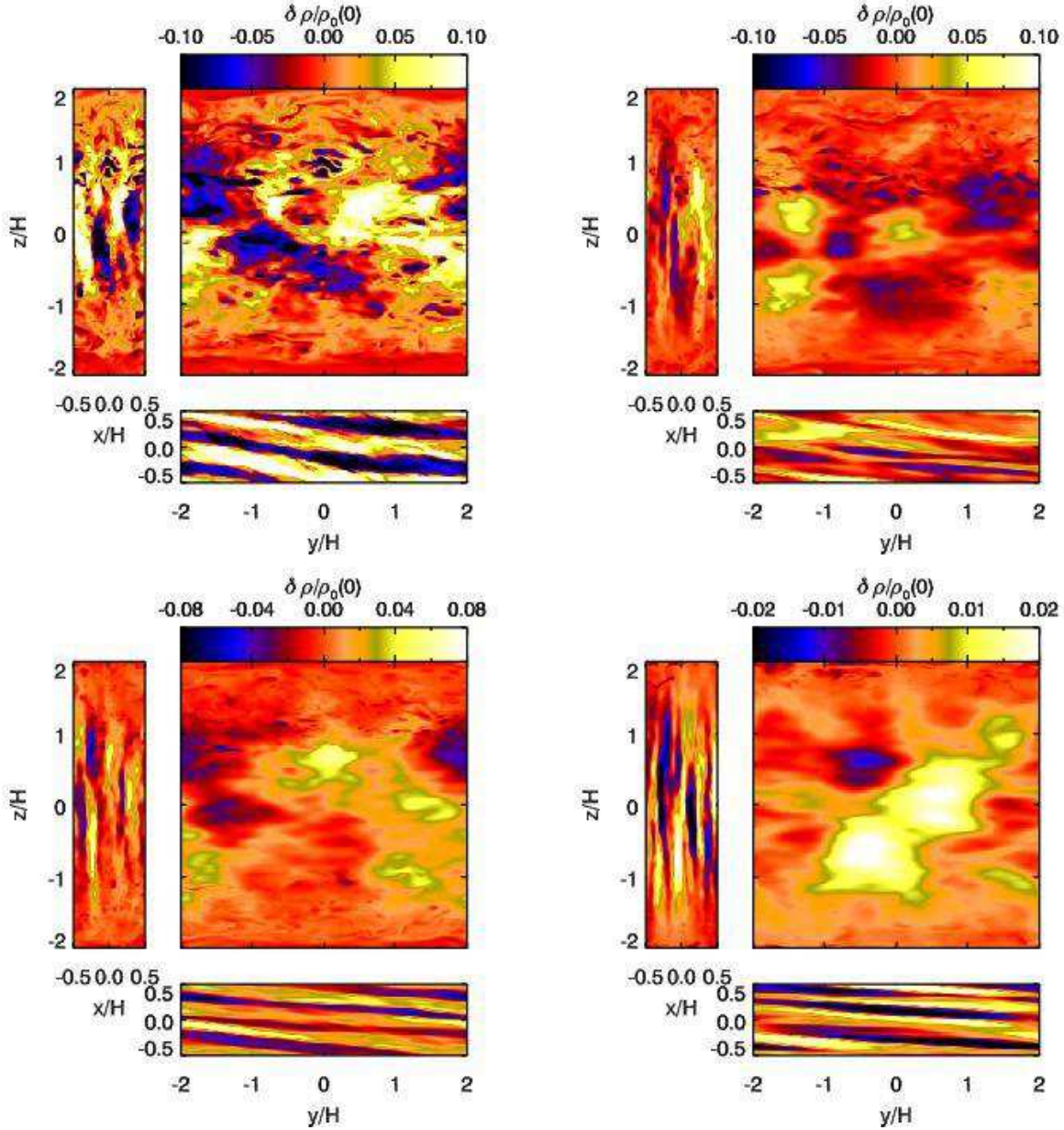


Fig. 11.— Turbulent overdensities $\delta\rho = \rho - \rho_0$, where ρ_0 is the initial hydrostatic distribution, in three orthogonal planes through the origin in each model with increasing dead zone width and normalized by the initial midplane density, $\rho_0(0)$. xz and yx cuts surround the yz cut. All sub-panels share a common color scale, given by the colorbar over the yz images. Clockwise from top left, $Re = \infty, 100, 30, 3$. As the dead zone width increases, a clear transition from turbulent to wave-like behavior is visible at the midplane.

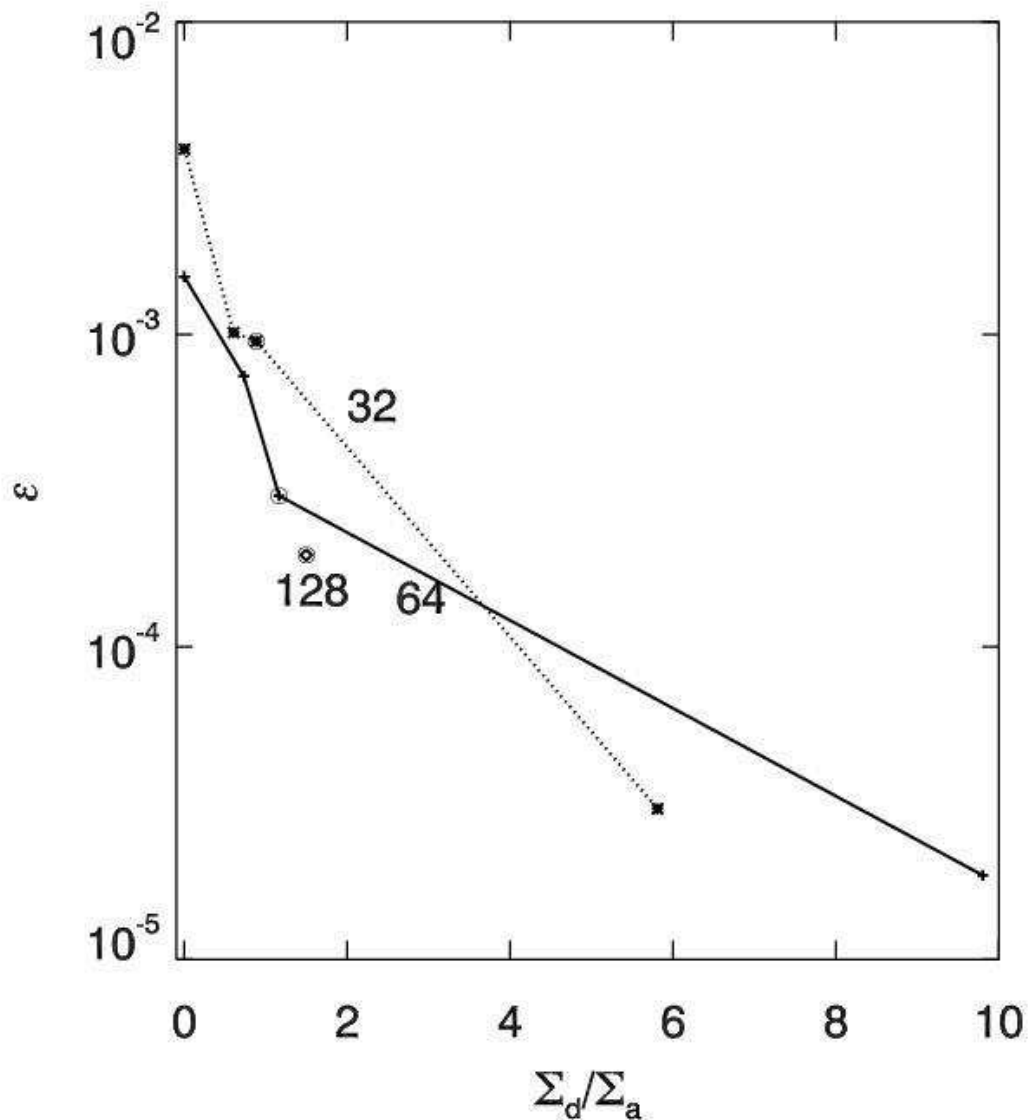


Fig. 12.— Derived diffusion parameter ϵ estimated from turbulent torques versus dead zone to active zone column density ratio Σ_D/Σ_A in all runs. Each resolution is labeled by its $N_x = 32, 64, 128$, corresponding to our low, medium, and high resolution runs. For the low and medium resolutions, there are several Re_M values; for the $N_x = 128$ case there is only one ($Re_M = 30$), marked by a diamond. The circled points correspond to the $Re_M = 30$ case at each resolution, allowing a resolution study for D versus Σ_D/Σ_A . The dead zone size should be more resolution dependent towards the right of the figure, as the active layers get thinner and thus increasing numbers of unstable modes are inadequately resolved.